Supporting Information

Polyoxovanadate-Based Supramolecular Vesicles for Enhancing Lithium-Sulfur Battery Performance under High Rates, High Loadings, and Subzero-Temperature Conditions

Yihai Song, Yi Feng, Chunhui Zhang, Jiayuan Zhang, Linlin Fan*, Yundong Cao, Hong Liu*, and Guanggang Gao

School of Materials Science and Engineering

University of Jinan

Jinan 250022, China.

*Corresponding authors

E-mail: mse_fanll@ujn.edu.cn (Linlin Fan); mse_liuh@ujn.edu.cn (Hong Liu)

1.1 Synthesis of V_{34}-DODA

$K_{10}[V_{34}O_{82}]\cdot 20H_2O$ (V_{34}) was synthesized using a previously reported method with further optimizations.[1,2] V_{34} was completely dissolved in water to obtain a black-green solution A. DODA was dissolved in chloroform to form a transparent solution B, where the molar ratio of DODA to V_{34} was controlled at 10 : 1. Solution A was slowly poured into solution B, and after stirring for 5 h of reaction, the aqueous phase turned colorless. The organic layer was separated, and an appropriate amount of ethanol was slowly added to it, followed by continuous stirring for 2 h. After that, the mixture was left to stand overnight, and the supernatant was decanted. The solid product was separated by centrifugation, washed three times with ethanol and water successively, and finally dried under vacuum for 12 h.

Based on the test results of ICP and EA, the mass fractions of C and V in V_{34}-DODA are 50.17% and 19.96%, respectively, and the calculated C/V mass ratio is 2.527. This measured value is highly close to the theoretical C/V mass ratio (2.635) calculated based on the chemical formula $(DODA)_{10}V_{34}$.

1.2 Preparation of V_{34}-DODA modified separator

V_{34}-DODA composite, Super P and polyvinylidene fluoride (PVDF) were combined in N-methyl-2-pyrrolidinone (NMP) at a mass ratio of 6:3:1 under vigorous stirring to generate a uniform slurry, which was then scraped on one side of the PP separator by using a doctor blade. The obtained functionalized separator was subjected to vacuum drying at 50 °C for a duration of 12 h and punched into a Ø20 mm circular membrane.

1.3 Preparation of C/S composite cathode

The C/S composite was prepared through a melt diffusion technique. Firstly, conductive C and sulfur powder were meticulously mixed in a 3:7 weight ratio using a mortar and pestle. Subsequently, the blend was heated at 155 °C for 12 h inside an argon-filled autoclave to synthesize the C/S composite.

C/S composite, Super P and PVDF were combined in NMP at a mass ratio of 7:2:1 under vigorous stirring to generate a uniform slurry, which was then scraped on one side of the Al foil by using a doctor blade. The obtained C/S composite cathode was

subjected to vacuum drying at 50 °C for a duration of 12 h and punched into a Ø10 mm circular. The areal loading of sulfur in the cathode is ~1.0 mg cm^{-2}. Meanwhile, we also increased the sulfur loading to ~4.0 mg cm^{-2} and ~6.6 mg cm^{-2}, respectively.

1.4 Synthesis of Li_2S_6 solution

Li_2S_6 solution was made by dissolving anhydrous lithium sulfide (Li_2S) and sublimed sulfur with a stoichiometric ratio of 1:5 in the organic solution of 1,3-Dioxolane (DOL) and 1,2-Dimethoxyethane (DME) (volume ratio is 1:1). And then the suspension was heated at 60 °C and stirred violently for 12 h under the protection of Argon gas to generate a Li_2S_6 solution with the atomic sulfur concentration of 0.5 M. Finally, the Li_2S_6 solution was diluted to a suitable concentration to carry out adsorption experiment.

1.5 Material characterization

The microstructures and elemental mappings of the prepared samples were examined using scanning electron microscopy equipped with X-ray energy dispersive spectroscopes (SEM, Zeiss, Gemini 300 and Oxford, X-Max^N 50). The structural compositions of the samples were identified through X-ray diffraction (XRD, Rigaku Ultima IV) utilizing Cu Kα radiation (50 kV). Fourier transform infrared (FTIR) spectroscopy was conducted using a NEXUS-870 spectrophotometer with KBr pellets. The chemical compositions and surface element states of the samples were analyzed using X-ray photoelectron spectroscopy (XPS, Thermo Scientific Escalab 250Xi, USA), with non-monochromatized Mg Kα X-rays serving as the excitation source. Additionally, ultraviolet-visible (UV-vis) spectrometry was conducted using a UV spectrophotometer (UV-8000S, Shanghai Yuanxi). Thermogravimetric (TG) analysis was conducted at a heating rate of 10 °C perminute using a TA Instrument Q600 Analyzer. Contact angles were measured using a POWEREACH JC2000D2G instrument. N_2 adsorption/desorption isotherms of the calcined catalysts was measured with SSA-6000107 instrument (Biaode, China). The contents of each element were determined by inductively coupled plasma spectroscopy (ICP, ICP-OES: Agilent 5110) and elemental analysis (EA, Elementar-UNICUBE).

1.6 Electrochemical measurements

For Li-S cells, V_{34}-DODA modified separators were employed, and the cell contained an electrolyte/sulfur ratio of 10 μL mg^{-1}. The electrolyte consisted of 1.0 M LiTFSI dissolved in a 1:1 volume ratio of DOL and DME, supplemented with 2.0 wt% $LiNO_3$. Each cell was filled with 30 μL of this electrolyte. The DH7006 electrochemical workstation from Jiangsu Donghua Analytical Instrument Co., Ltd. (Donghua Analytical) was employed to conduct electrochemical impedance spectroscopy (EIS) measurements. The EIS tests were performed in the frequency range of 100 kHz to 0.01 Hz with a voltage amplitude of 10 mV. The cycle performance and rate performance of the Li-S cells were evaluated using the Neware battery test system (CT-4008-Tn-5V50mA-164, Shenzhen Neware Electronics Co., Ltd., China). All the aforementioned CR2032-type cells were assembled in an argon-filled glove box, maintaining an oxygen level below 0.1 ppm and a water content below 0.1 ppm.

1.7 Low-temperature performance test

Li-S batteries are assembled with PP separator or V_{34}-DODA modified separator and kept standing at room temperature for 8 h to achieve sufficient electrolyte infiltration. The batteries are then transferred to a thermostat chamber set at −10 °C or −20 °C and held for another 2 h to reach thermal equilibrium. Cyclic performance tests are subsequently conducted at the corresponding temperature.

1.8 Lithium ion transference number test

The process involves assembling symmetric Li//Li symmetric cells with PP or modified separator, and subsequently measuring the lithium-ion transfer number utilizing an electrochemical workstation (DH7006). The constant step polarization potential was 10 mV and the lithium ion transference number was defined as the ratio of steady-state current to initial-state current according to the following Bruce-Vincent-Evans equation:

$$t_{Li}{}^{+} = \frac{I_s(\Delta V - I_0 R_0)}{I_0(\Delta V - I_s R_s)} \quad (1)$$

Where R_0 and R_s refer to the initial and steady-state electrode|electrolyte interfacial resistances, respectively; I_0 and I_s represent the current values in initial and steady-state, respectively; t_{Li^+} is the lithium ion transference number.

1.9 Ionic conductivity test

The ionic conductivity of the electrolyte-soaked separators was tested with two stainless steels (SS) blocking cells (SS//separator//SS) by EIS in the frequency range from 1000 kHz to 0.01 Hz on the DH7006 electrochemical workstation. The ionic conductivity was calculated according to the following relation equation:

$$\sigma = \frac{l}{R_b A} \tag{2}$$

Where σ represents the ionic conductivity, l signifies the thickness of the separator, R_b stands for the resistance, and A is the effective area of electrodes, respectively.

1.10 Galvanostatic intermittent titration technique (GITT) test

Before testing, the batteries were rested under open circuit voltage for 10 h. The specific procedures were as follows: first, a 0.1 C current pulse was applied for 20 min, followed by a 30 min rest relaxation process. The polarization during electrochemical operation was quantified by introducing both internal resistance parameters and the Li^+ diffusion coefficients, with their correlation mechanisms described as follows:

$$\Delta R_{internal}(\Omega) = \frac{\left|\Delta_{QOCV-CVV}\right|}{I_{applied}} \tag{3}$$

Where ΔV is the voltage difference between the quasi-open circuit voltage (QOCV) and the closed circuit voltage (CCV), and Iapplied is the applied current.

$$D_{Li^+} = \frac{4L^2}{\pi\tau}\left(\frac{\Delta E_s}{\Delta E_t}\right)^2 \tag{4}$$

Herein, τ represents the current pulse time (s), ΔE_s signifies the deviation of individual equilibrium voltage, ΔE_t denotes the voltage deviation during the current pulse, and L is the average electrode thickness (cm).

1.11 Potentiostatic nucleation of Li_2S

The preparation method of lithium octasulfide (Li_2S_8) electrolyte is as follows: it is

synthesized by reacting S with anhydrous lithium sulfide (Li_2S) at a molar ratio of 1:7 in a 1:1 volume ratio of DOL and DME. The electrode preparation process is described as follows: catalyst materials (V_{34}, DODA, and V_{34}-DODA) are uniformly mixed with a PVDF binder at a mass ratio of 9:1, and the mixture is coated onto the surface of carbon-coated aluminum foil (diameter: 10 mm); the areal loading of the catalyst material in the cathode is controlled at approximately 0.5 mg cm^{-2}.

During battery assembly, 25 μL of the aforementioned Li_2S_8 electrolyte is dropped onto the cathode side, and 25 μL of conventional electrolyte is injected onto the lithium foil anode side. The assembled battery is first discharged at a constant current of 0.112 mA to 2.04 V, followed by a constant-potential discharge at 2.03 V until the current drops below 0.01 mA. According to Faraday's law, the nucleation capacity of Li_2S can be calculated by integrating the area under the obtained curve.

1.12 Density functional theory (DFT) calculations

The calculations were performed within the framework of DFT, by using the projector augmented wave method as implemented in the Vienna ab Initio Simulation Package. The exchange-correlation energy was in the form of Perdew-Bruke-Ernzerhof. The cutoff energy for the plane-wave basis set was 500 eV, and 2×2×1 Γ-centered k-point grids were used for the Brillouin zone integrations. For the surface systems, the bottom atom layers were fixed to simulate the body state, while the top atom layers were free to simulate the surface state. To reduce the interactions between each surface, a vacuum of 20 Å was contained in our calculation models. All structures were fully relaxed to the optimized geometry with the force convergence set at 0.01 eV $Å^{-1}$. To investigate the lowest energy configurations of adsorbed systems, we carefully manipulated structure parameters of the initial state (the distance, angle, and displacement between molecule and surface) to fully relax and selected the lowest energy result as the final state. Herein, the binding energy (E_{ads}) is defined as:

$$E_{ads} = E_{total} - E_{V_{34}} - E_{LiPSs}$$

Where E_{total} is the total energy of V_{34} combined with lithium polysulfides (LiPSs), E_{V34} is the surface energy of V_{34}, and E_{LiPSs} represents the energy of LiPSs in vacuum.

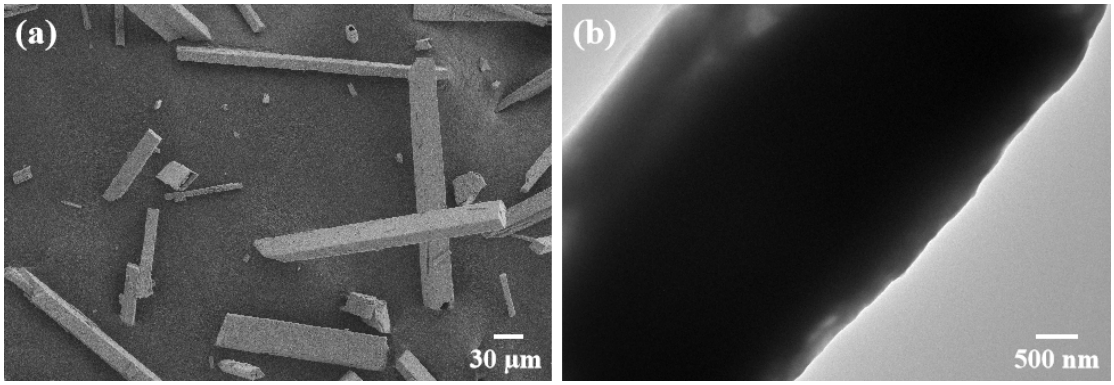

Fig. S1. (a) SEM and (b) TEM images of pristine V_{34}.

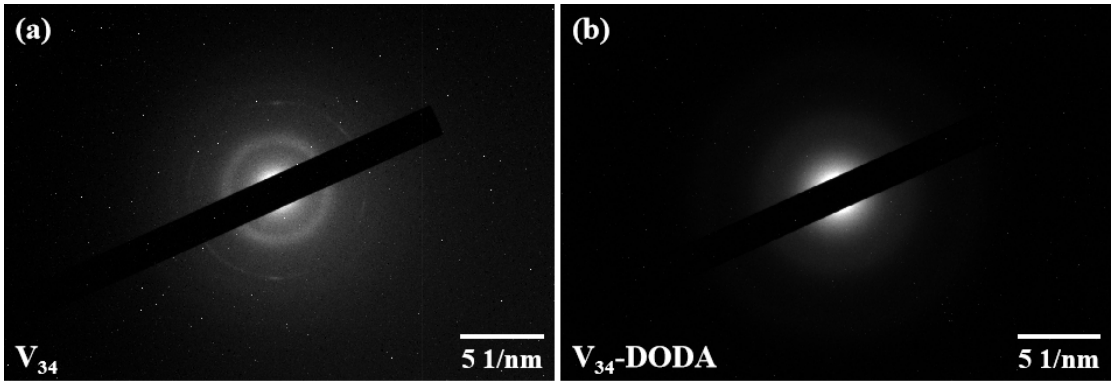

Fig. S2. SAED pattern of (a) pristine V_{34} and (b) V_{34}-DODA.

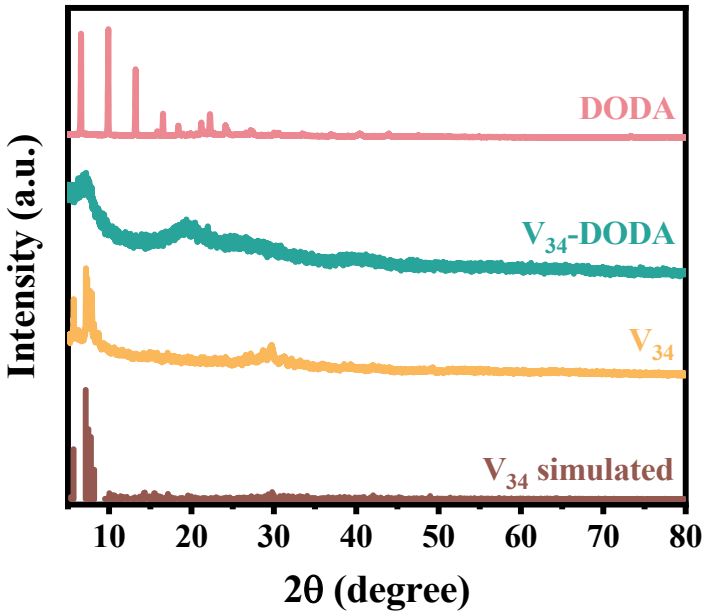

Fig. S3. XRD pattern of V_{34}, DODA, and V_{34}-DODA.

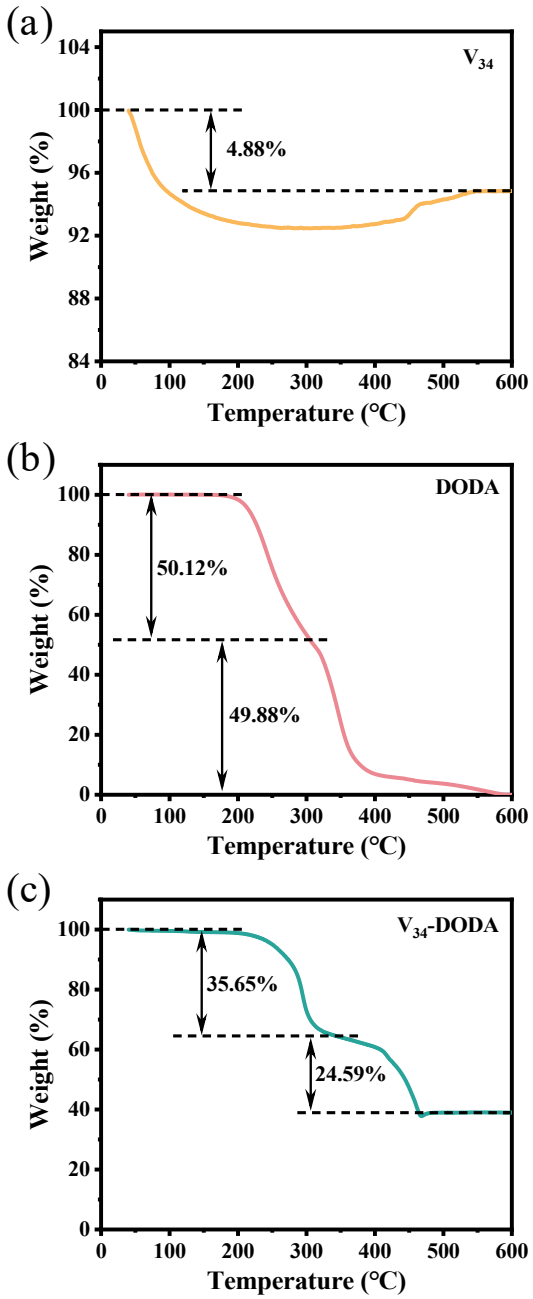

Fig. S4. TGA curves of (a) V_{34}, (b) DODA, and (c) V_{34}-DODA.

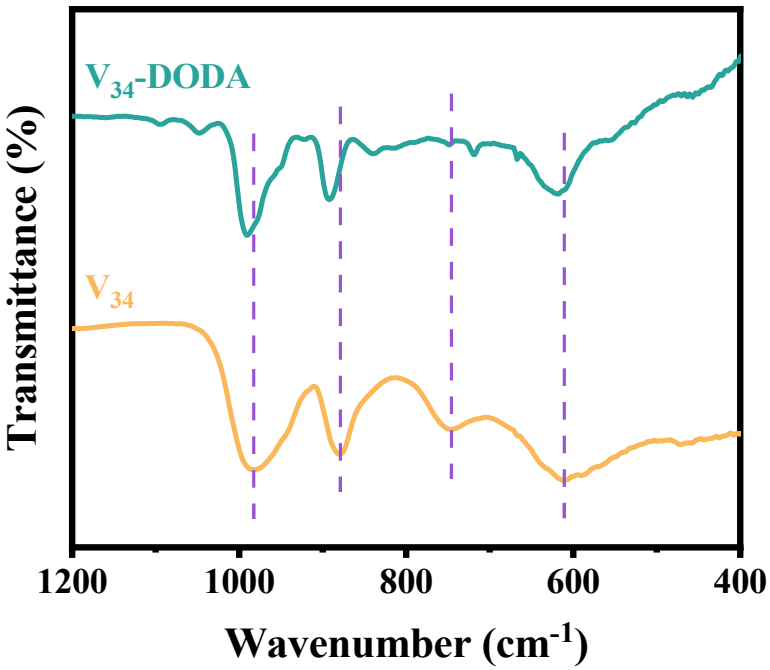

Fig. S5. FTIR spectra of V_{34} and V_{34}-DODA.

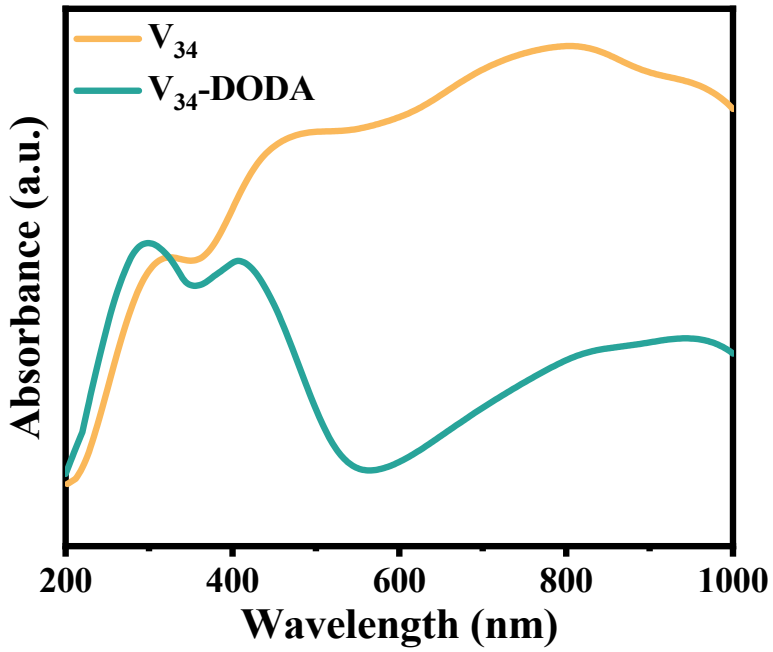

Fig. S6. UV-visible diffuse reflection spectra for V_{34} and V_{34}-DODA.

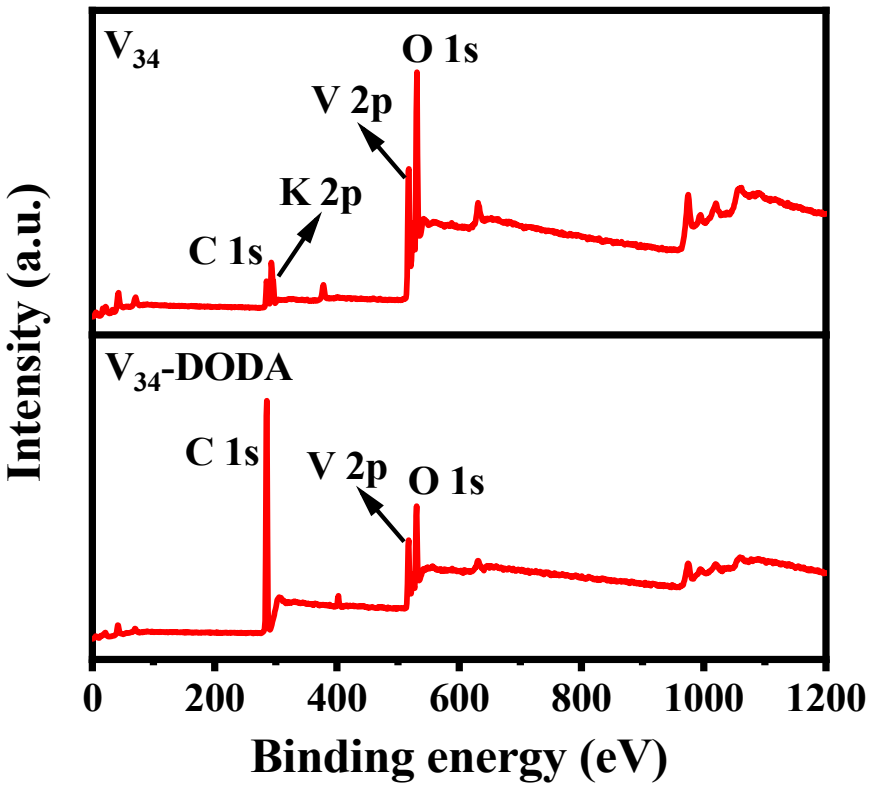

Fig. S7. The survey spectra XPS analysis of V_{34} and V_{34}-DODA.

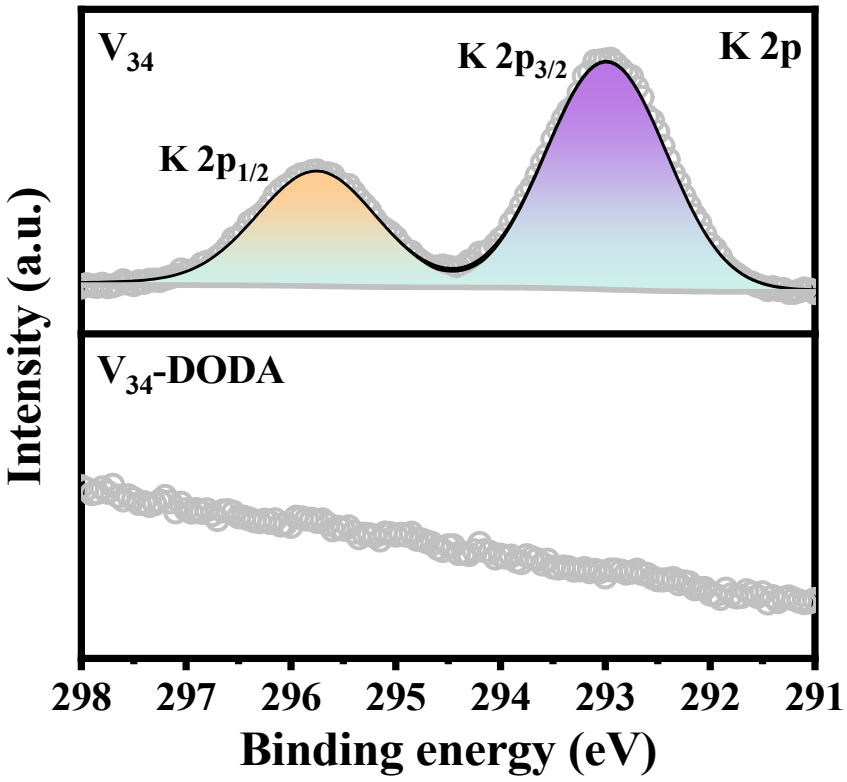

Fig. S8. The high-resolution XPS K 2p regional spectra of V_{34} and V_{34}-DODA.

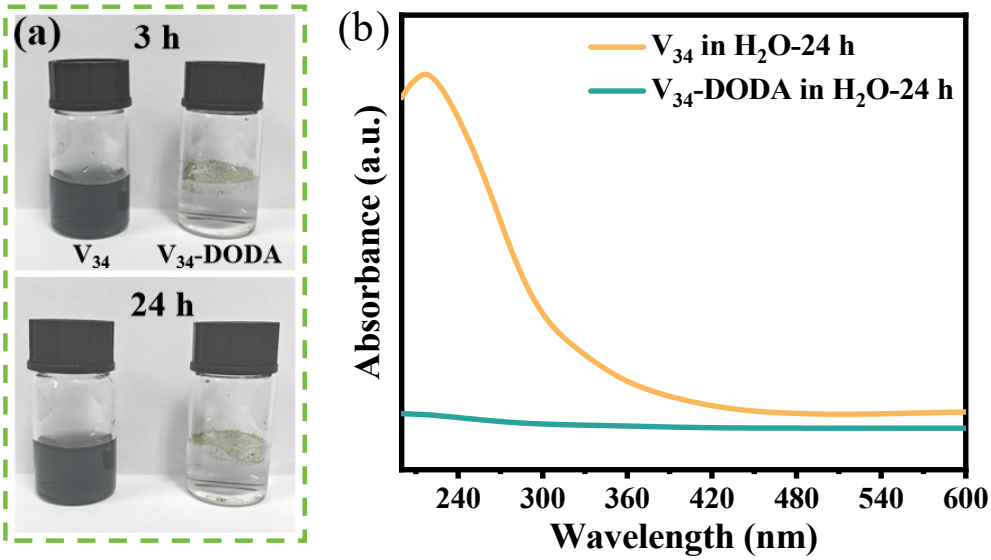

Fig. S9. (a) Observation of solubility of V_{34} and V_{34}-DODA powder in H_2O, and (b) corresponding UV-vis spectra of the supernatant.

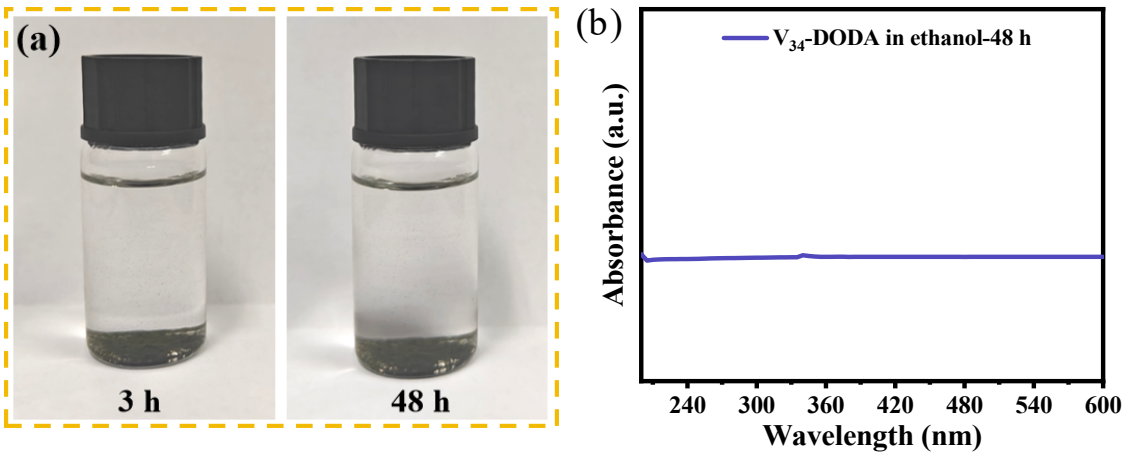

Fig. S10. (a) Observation of solubility of V_{34}-DODA powder in ethanol, and (b) corresponding UV-vis spectra of the supernatant.

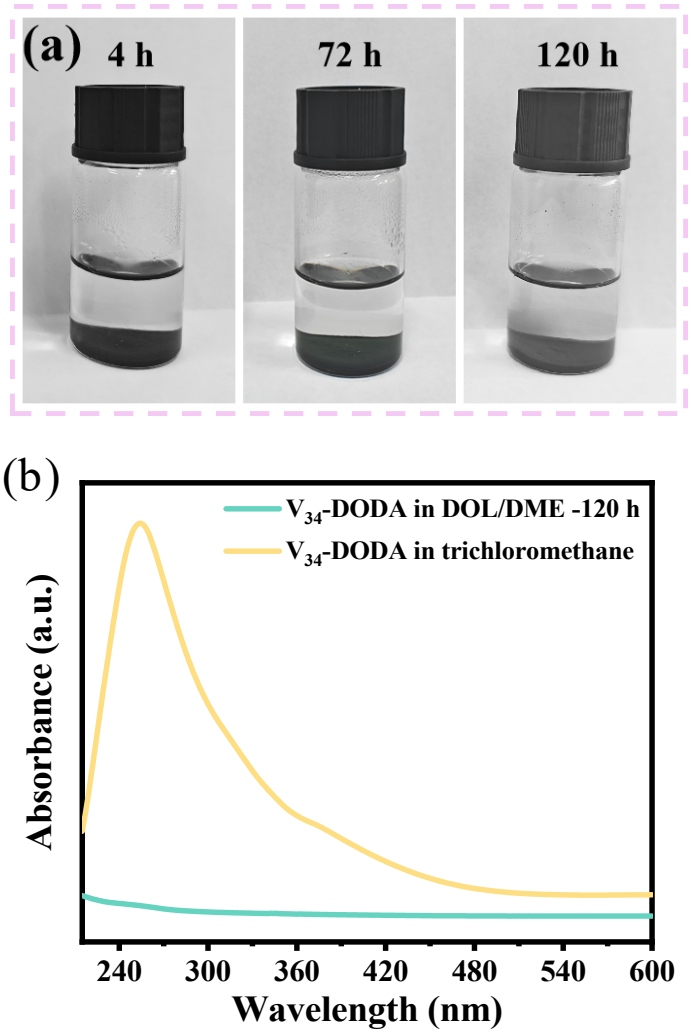

Fig. S11. (a) Observation of solubility of V_{34}-DODA powder in electrolyte (1:1 volume ratio of DOL and DME), and (b) corresponding UV-vis spectra of the supernatant.

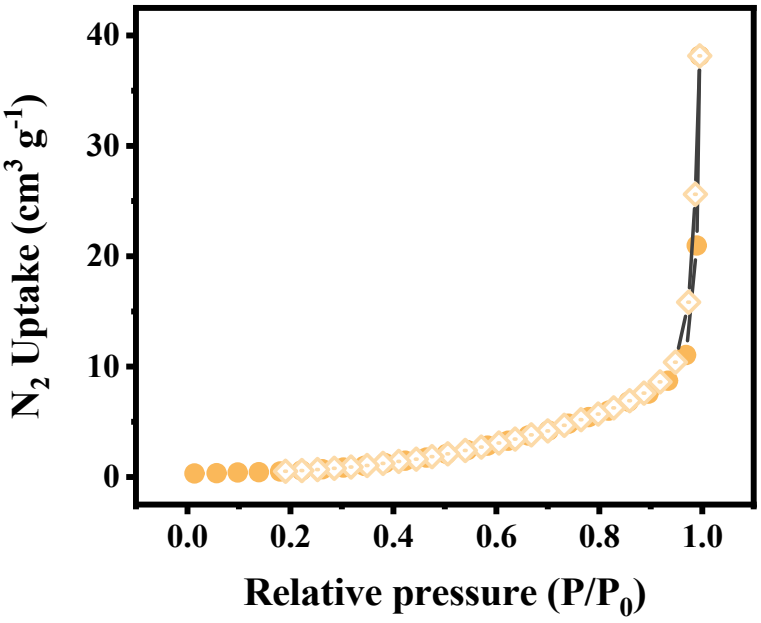

Fig. S12. Nitrogen adsorption-desorption isotherms of V_{34}.

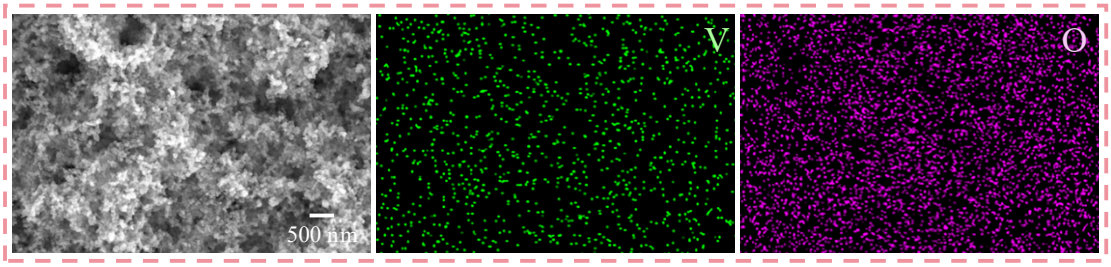

Fig. S13. The top-surface EDS mappings of the V_{34}-DODA modified separator.

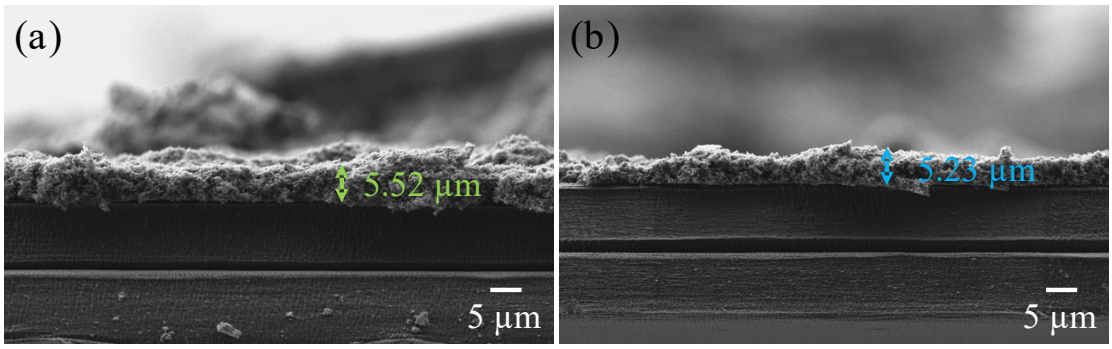

Fig. S14. Cross-sectional SEM images of (a) V_{34} modified separator and (b) DODA modified separator.

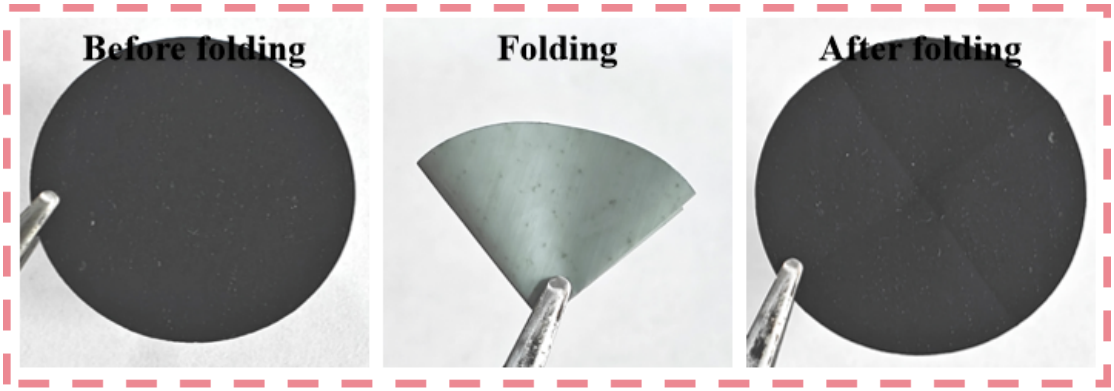

Fig. S15. The folding process photographs of the V_{34}-DODA modified separator.

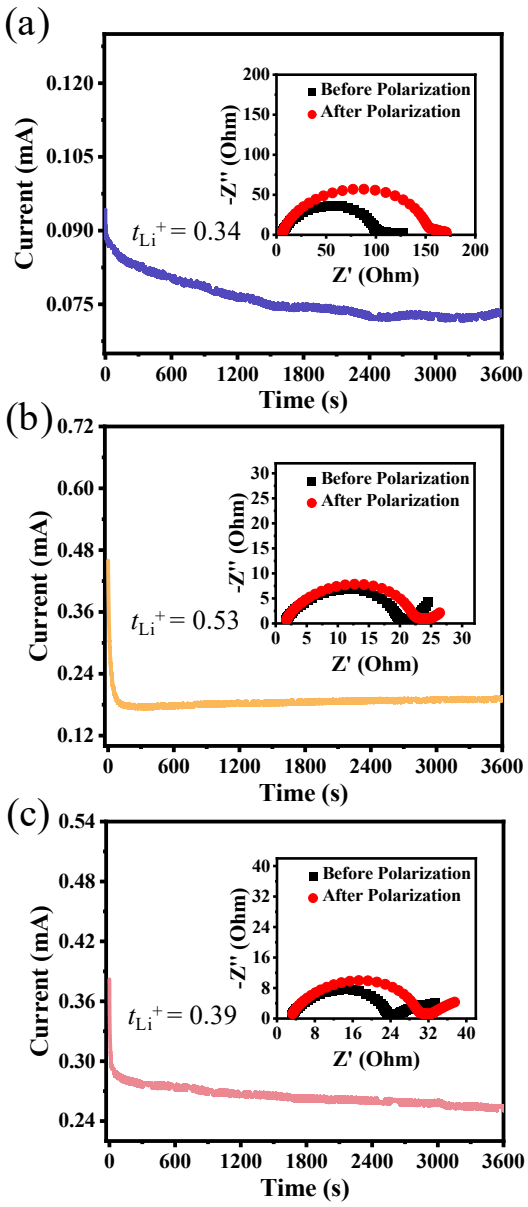

Fig. S16. Steady-state current under 10 mV polarization for symmetric cells with (a) PP separator, (b) V_{34} modified separator, and (c) DODA modified separator (inset: EIS measurements before and after polarization).

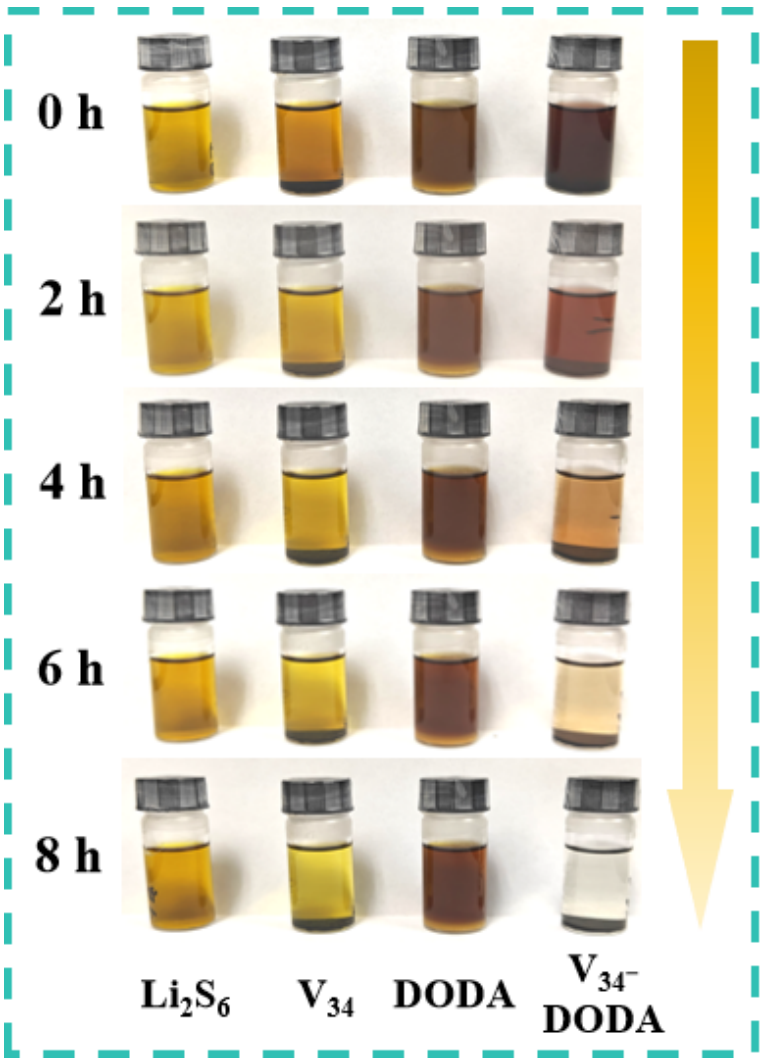

Fig. S17. Optical observation of Li_2S_6 solution adsorbed by V_{34}, DODA, and V_{34}-DODA powders.

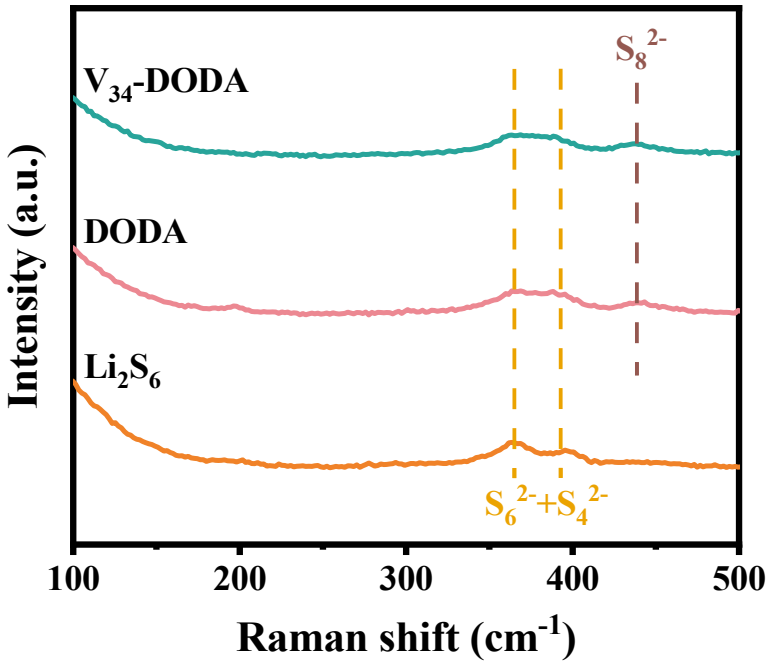

Fig. S18. Raman spectra of the Li_2S_6 solution after 1 h adsorption by DODA and V_{34}-DODA.

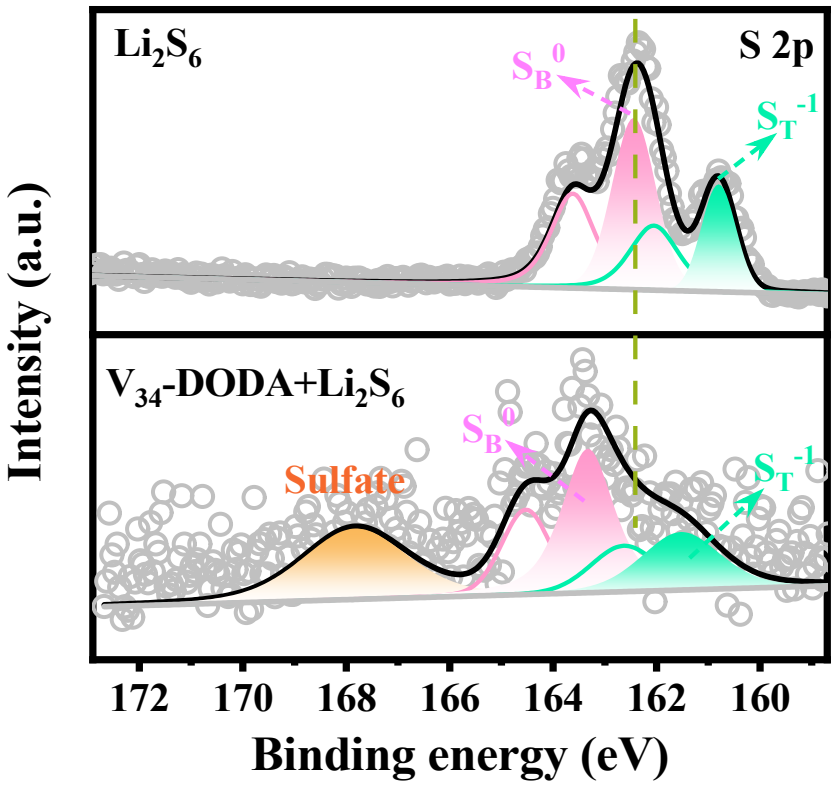

Fig. S19. S 2p XPS regional spectrum of V_{34}-DODA after adsorbing Li_2S_6.

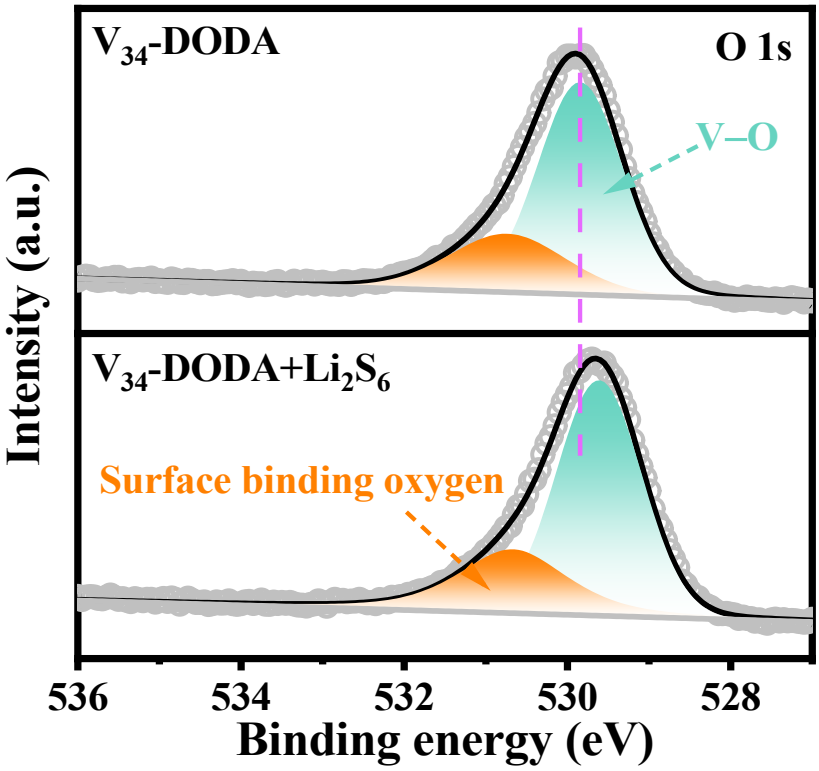

Fig. S20. O 1s XPS regional spectrum of V_{34}-DODA after adsorbing Li_2S_6.

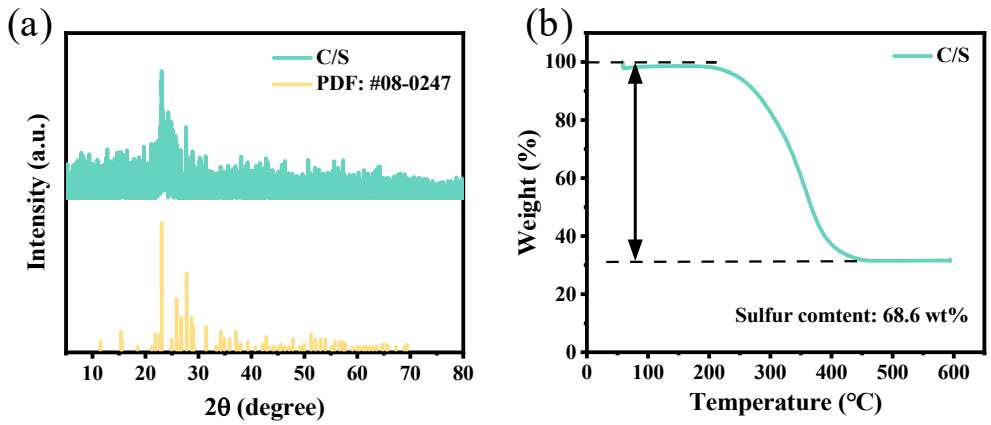

Fig. S21. (a) XRD pattern and (b) TGA curve of C/S composite.

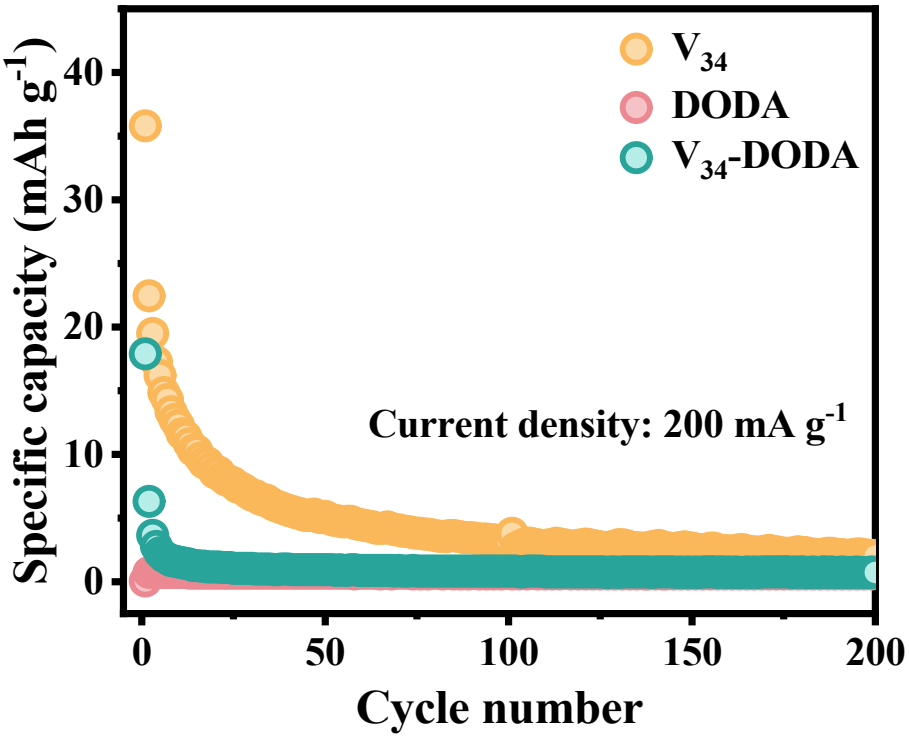

Fig. S22. Cycle performance of the cell with V_{34}, DODA, and V_{34}-DODA electrode at 200 mA g^{-1} in the voltage range of 1.7-2.8 V. The electrode is composed of 70 % sample, 20 % super P, and 10 % PVDF by weight.

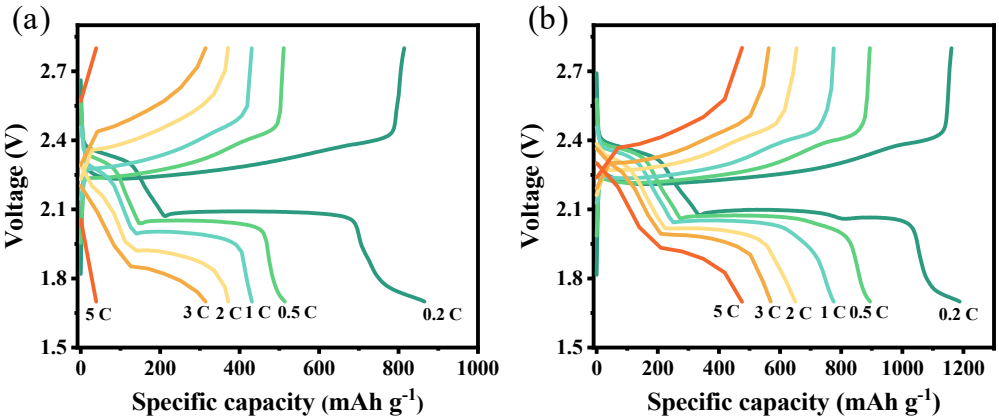

Fig. S23. Charge/discharge voltage profiles at different current densities for Li-S cells with (a) PP separator and V_{34}-DODA modified separator.

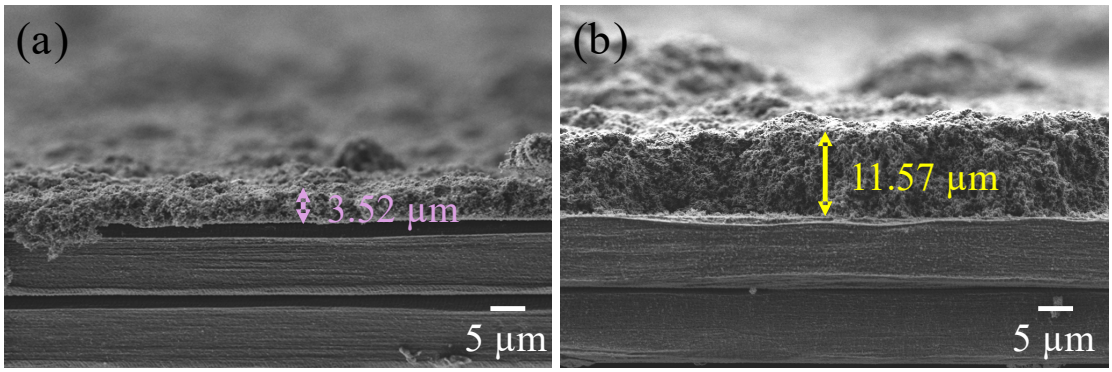

Fig. S24. The cross-sectional SEM images of V_{34}-DODA modified separators with different thicknesses.

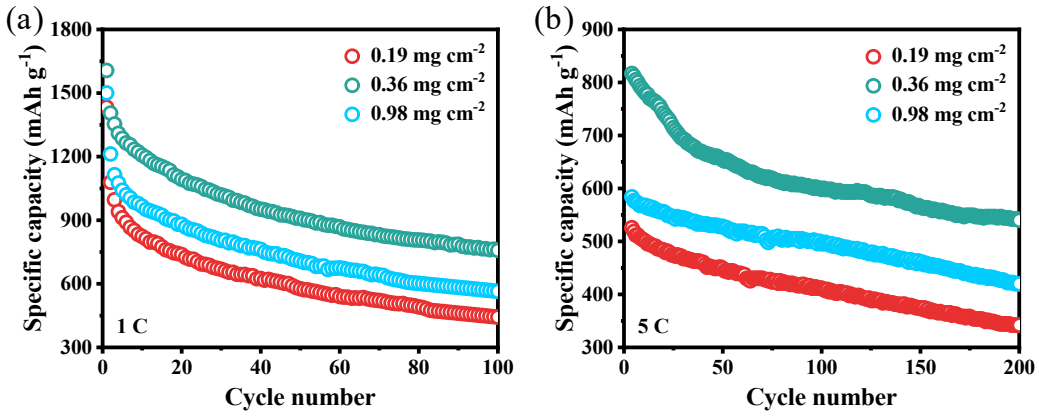

Fig. S25. Performance comparison of Li-S cells using V_{34}-DODA modified separators with different thicknesses at (a) 1 C and (b) 5 C.

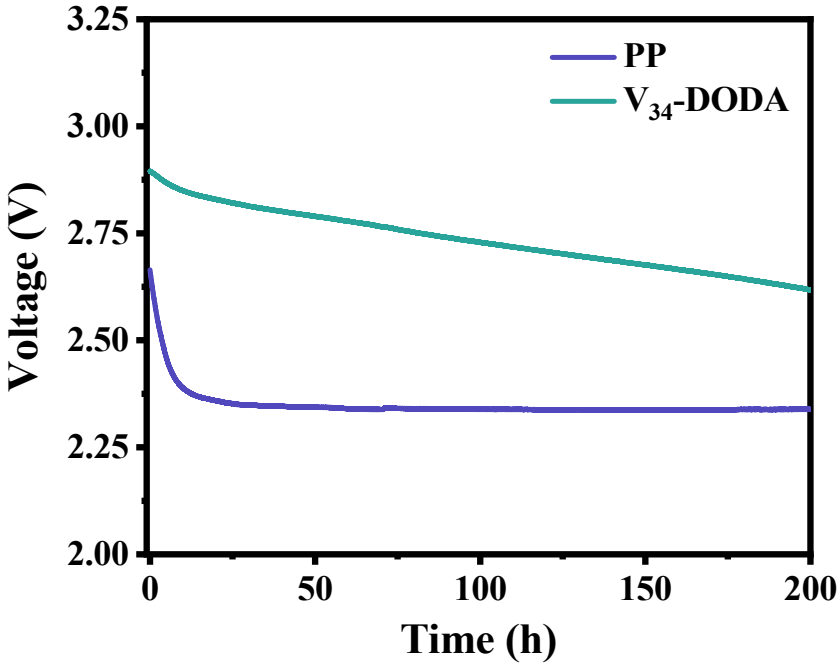

Fig. S26. Self-discharge behavior of Li-S cells with PP separator and V_{34}-DODA modified separator.

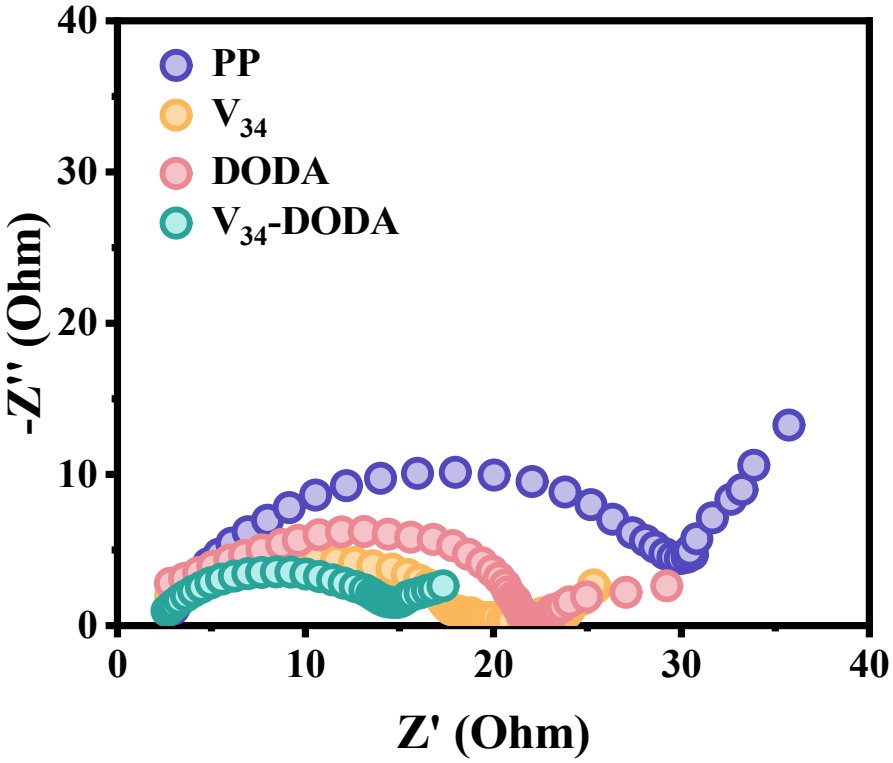

Fig. S27. Nyquist curves of Li-S cells with PP separator, V_{34} modified separator, DODA modified separator, and V_{34}-DODA modified separator.

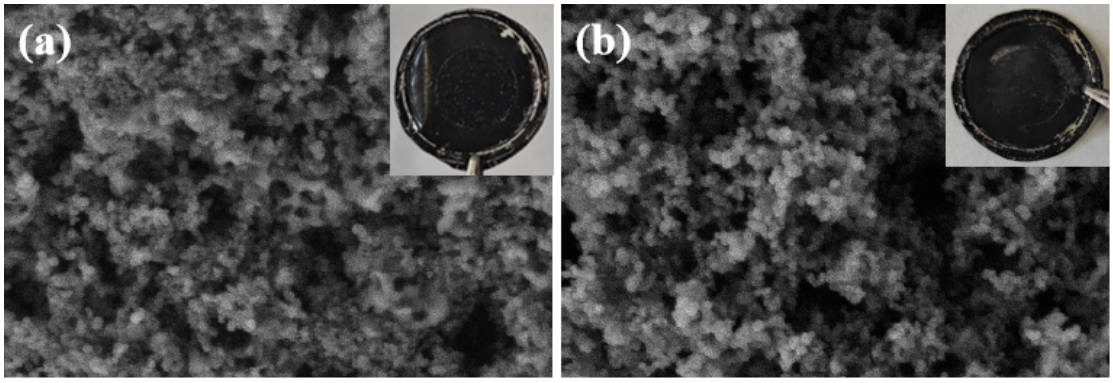

Fig. S28. The surface morphologies of V_{34}-DODA modified separator after (a) 50 cycles and (b) 100 cycles at 1 C.

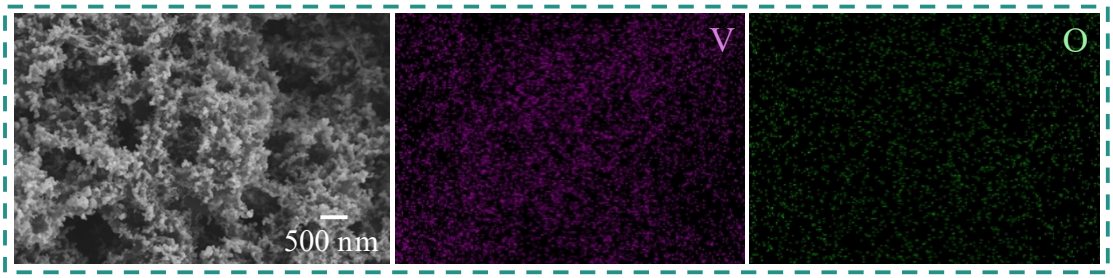

Fig. S29. Elementary mapping images of V_{34}-DODA modified separator after 100 cycles at 1 C.

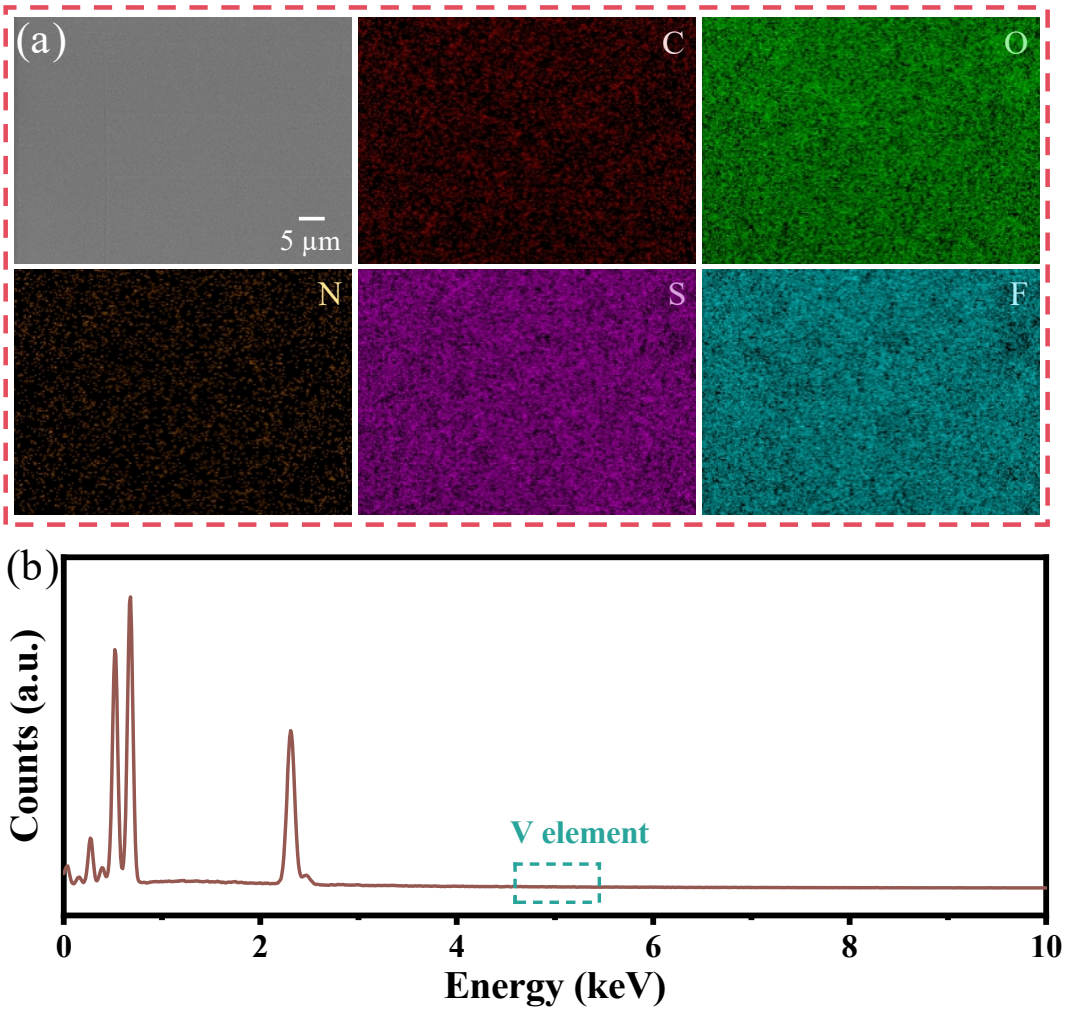

Fig. S30. (a) Elemental mapping and (b) EDS spectrum of the lithium metal anode after 100 cycles at 1 C. .

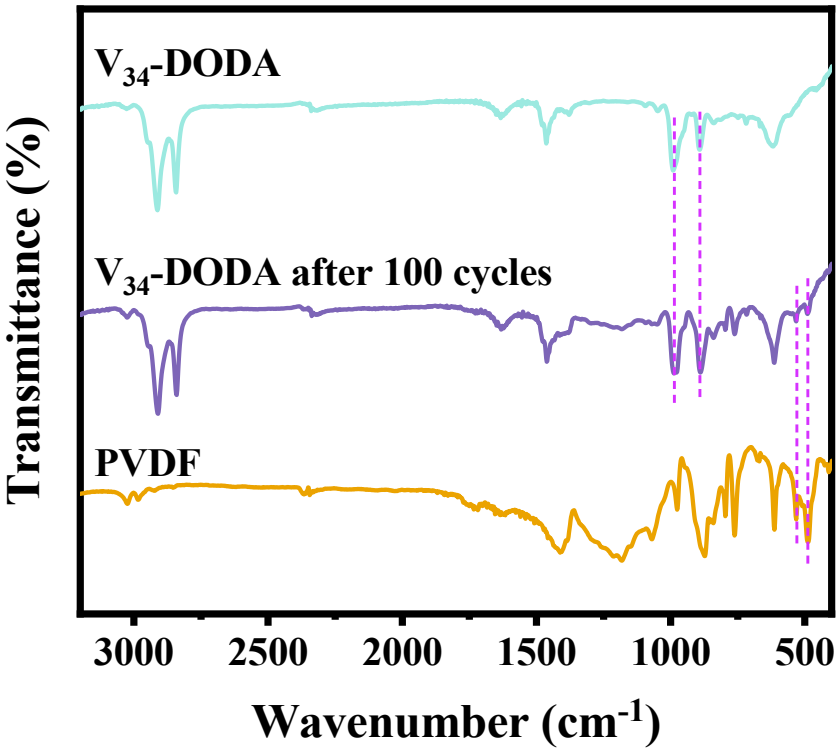

Fig. S31. FTIR analysis of the V_{34}-DODA modified separator after 100 cycles at 1 C.

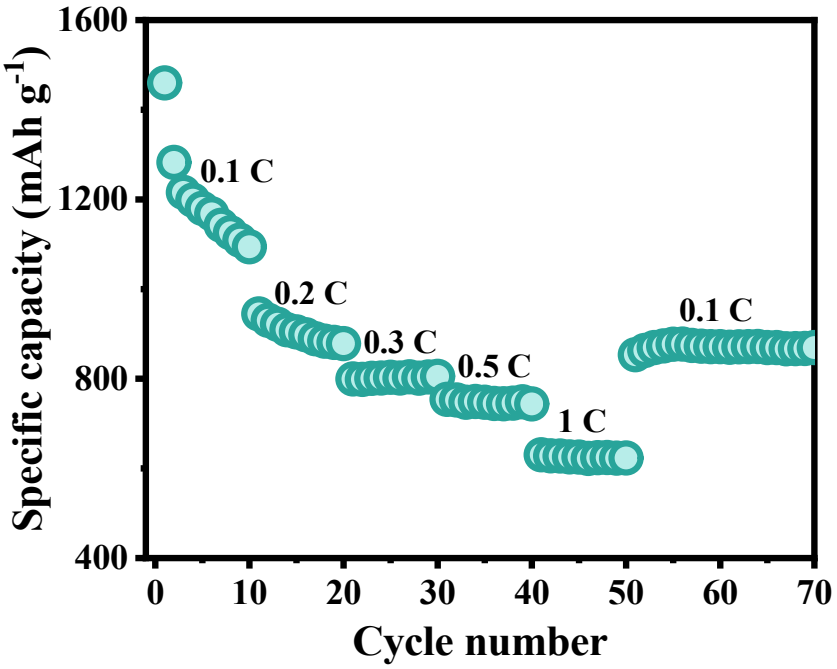

Fig. S32. Rate capability of Li-S cell with V_{34}-DODA modified separator at different current densities (sulfur loading: 4.0 mg cm^{-2}).

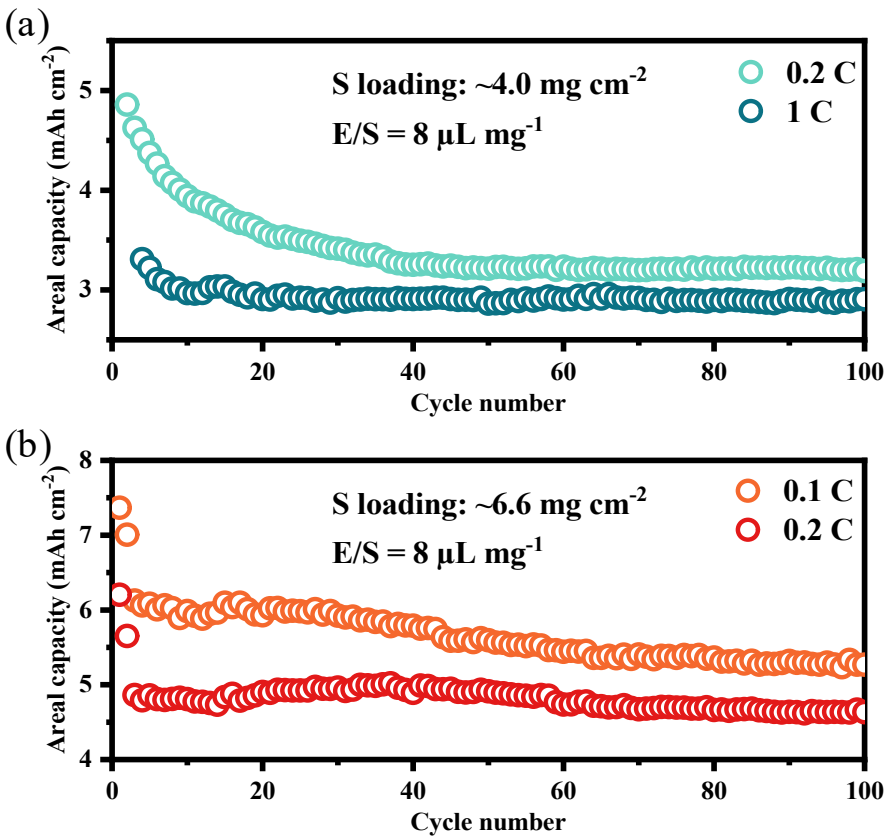

Fig. S33. Cycling performance of Li-S cells with V_{34}-DODA modified separators at sulfur loadings of (a) 4.0 mg cm^{-2} and (b) 6.6 mg cm^{-2}.

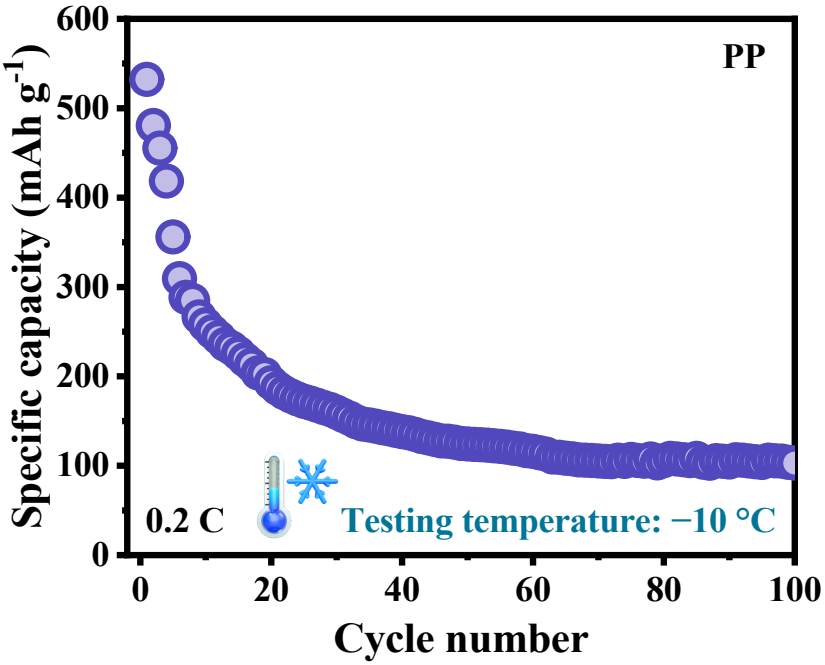

Fig. S34. Cycling performance of Li-S cell employing PP separator at 0.2 C under −10 °C (sulfur loading: 1.0 mg cm^{-2}).

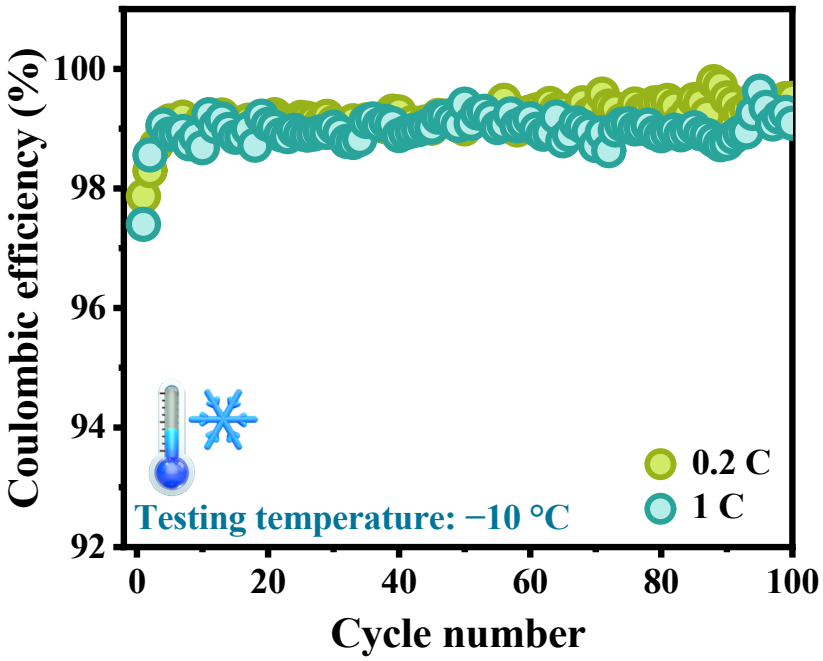

Fig. S35. Testing temperature at −10 °C, CE of the cell with V_{34}-DODA modified separator at both 0.2 C and 1 C.

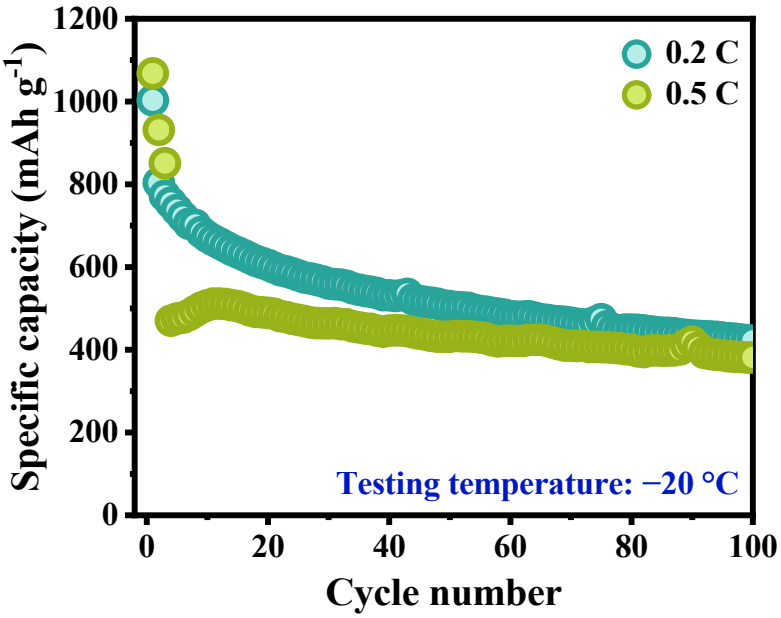

Fig. S36. Cycling performance of Li-S cells employing the V_{34}-DODA modified separator at both 0.2 C and 0.5 C under −20 °C (sulfur loading: 1.0 mg cm^{-2}).

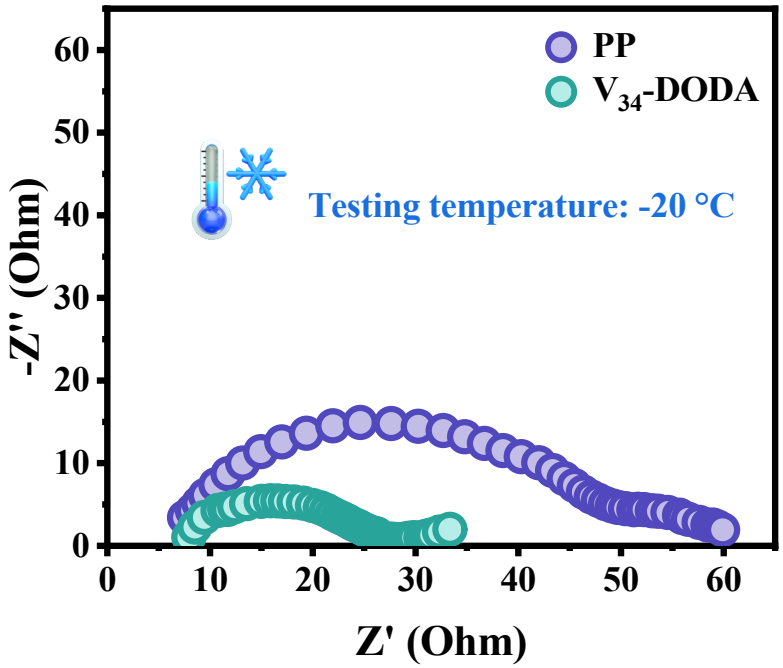

Fig. S37. Nyquist curves of Li-S cells with PP separator and V_{34}-DODA modified separator under −20 °C.

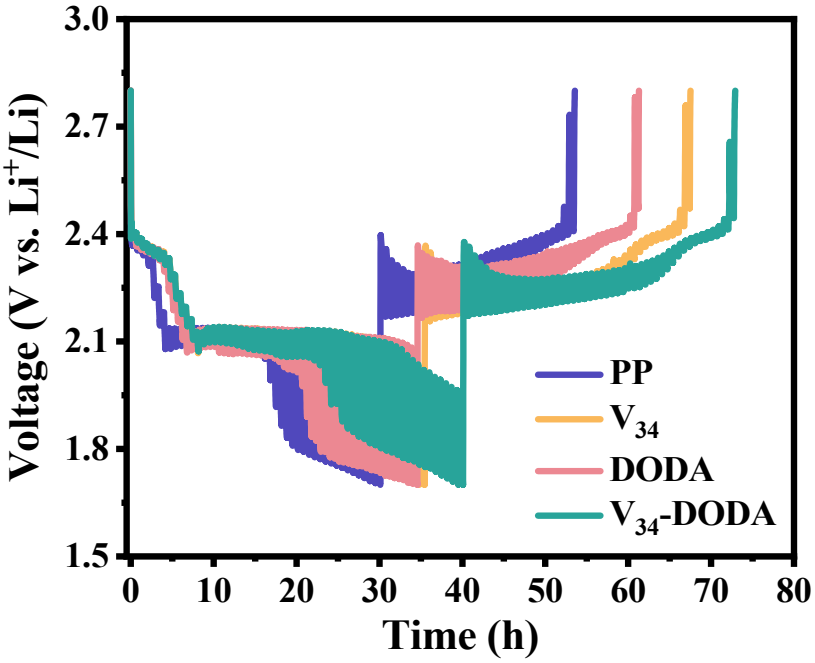

Fig. S38. GITT voltage profiles of Li-S cells with PP separator, V_{34} modified separator, DODA modified separator, and V_{34}-DODA modified separator.

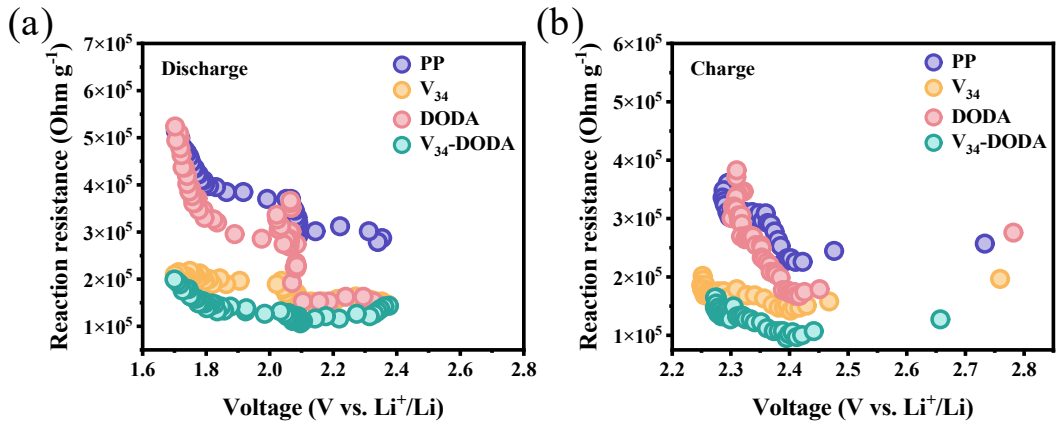

Fig. S39. The calculated reaction resistances based on GITT during the discharge (a) and charge (b) processes.

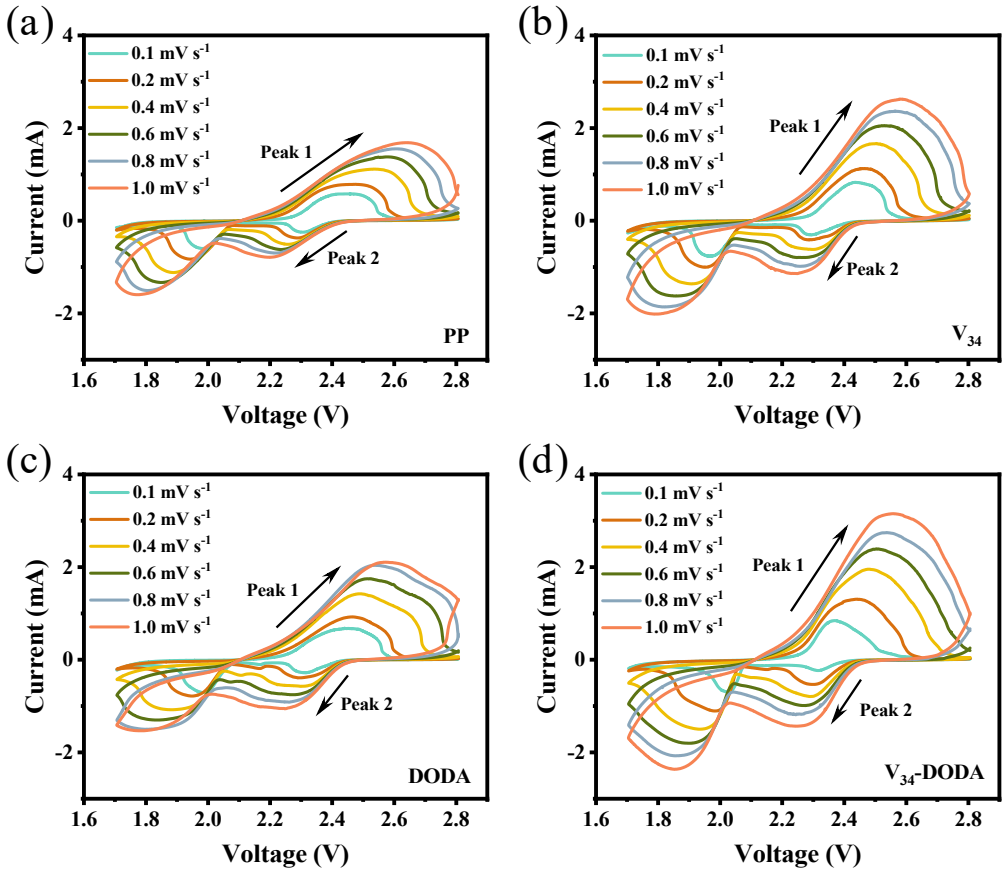

Fig. S40. Cyclic voltammetry of Li-S cells with (a) PP separator, (b) V_{34} modified separator, (c) DODA modified separator, and V_{34}-DODA modified separator at voltage from 1.7 V to 2.8 V under different scanning rates.

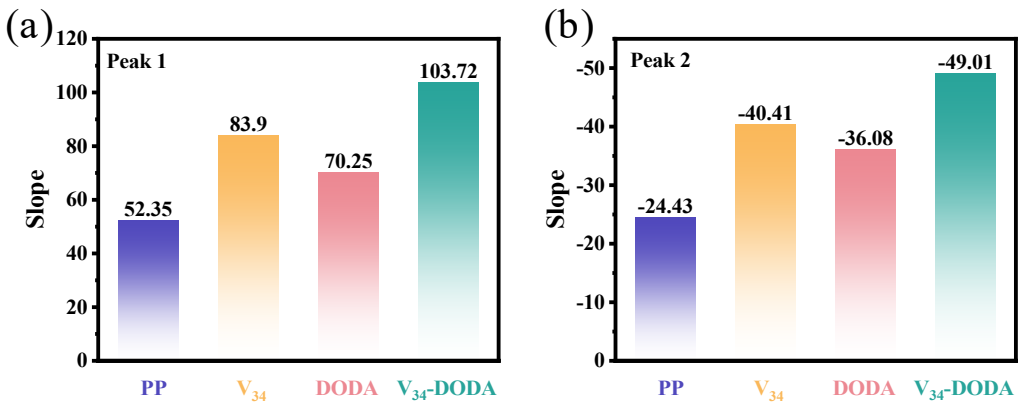

Fig. S41. Comparison diagram of slopes of $I_p/v^{1/2}$ curve for cells with V_{34}, DODA, and V_{34}-DODA modified separators: (a) peak 1 and (b) peak 2.

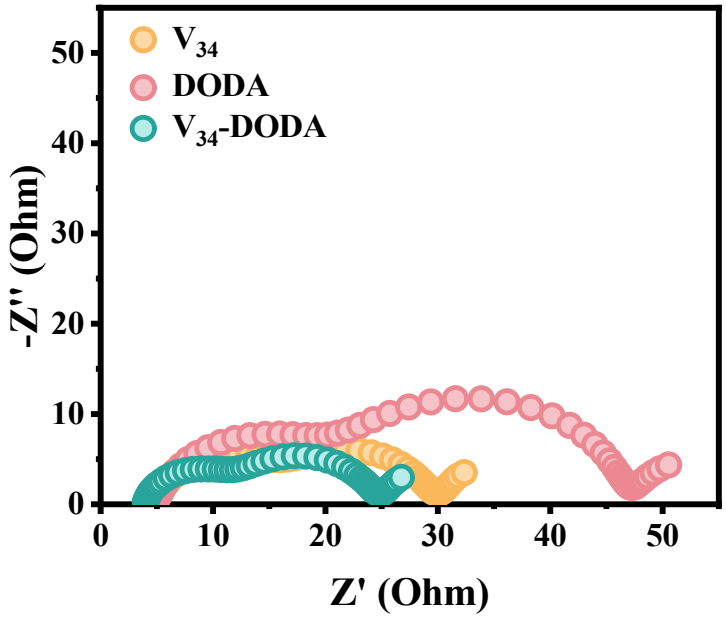

Fig. S42. EIS spectra of symmetric cells using V_{34}, DODA, and V_{34}-DODA electrodes.

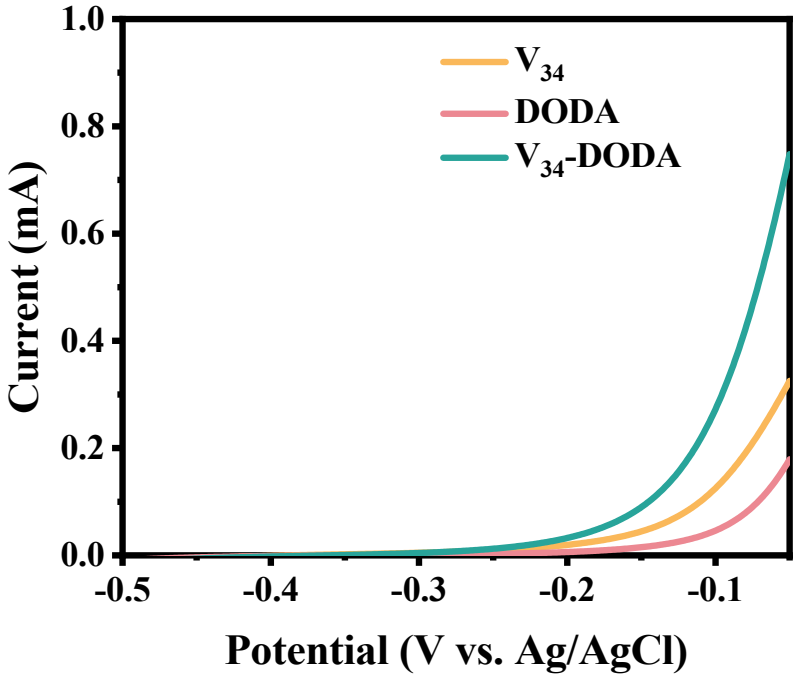

Fig. S43. LSV curves of sulfide oxidation reaction using V_{34}, DODA, and V_{34}-DODA electrodes.

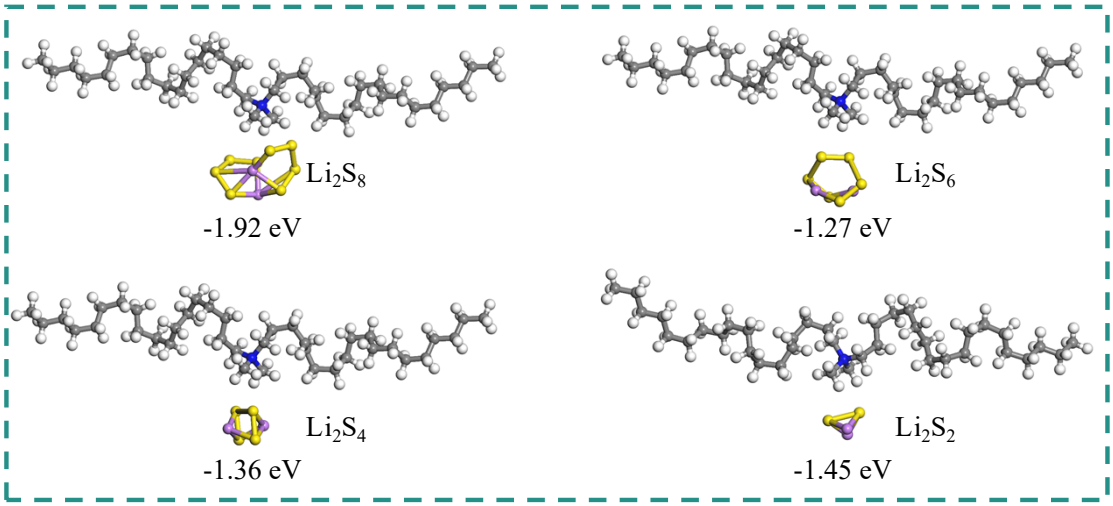

Fig. S44. The adsorption structures and corresponding adsorption energies of Li_2S_n on DODA. Color codes: S, yellow; Li, violet; C, gray; H, white; N, blue.

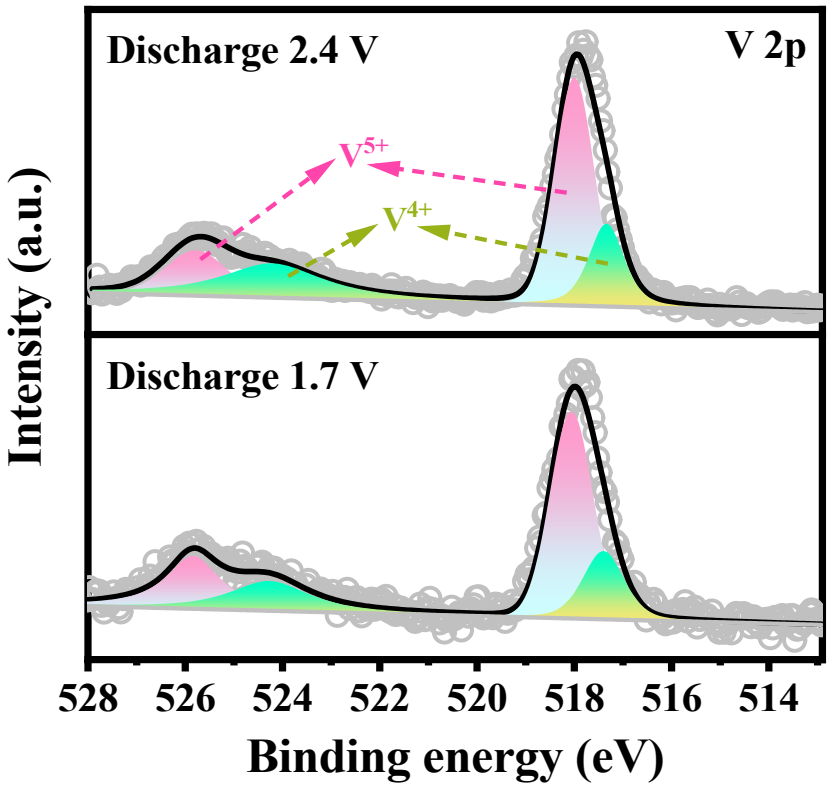

Fig. S45. V 2p XPS spectra for the first discharge process.

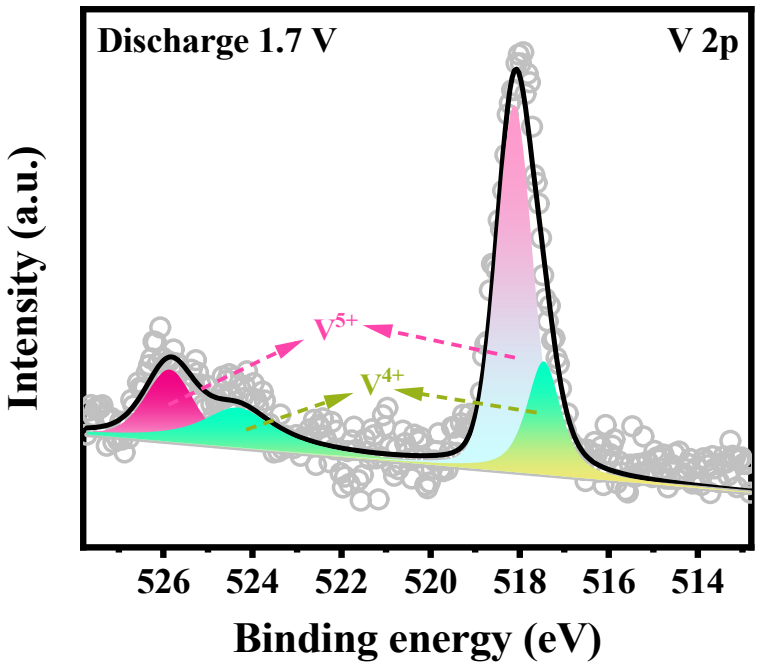

Fig. S46. V 2p XPS spectra for the second discharge process.

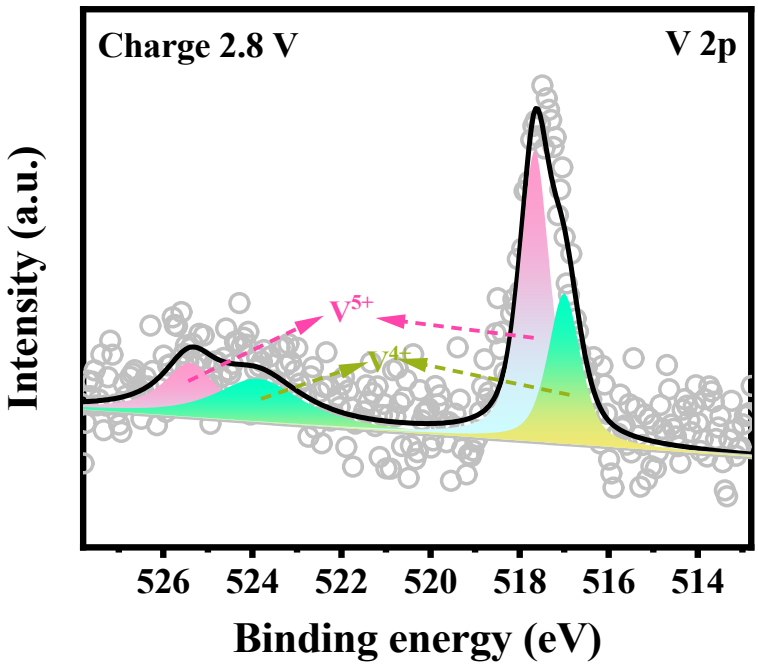

Fig. S47. V 2p XPS spectra for the second charge process.

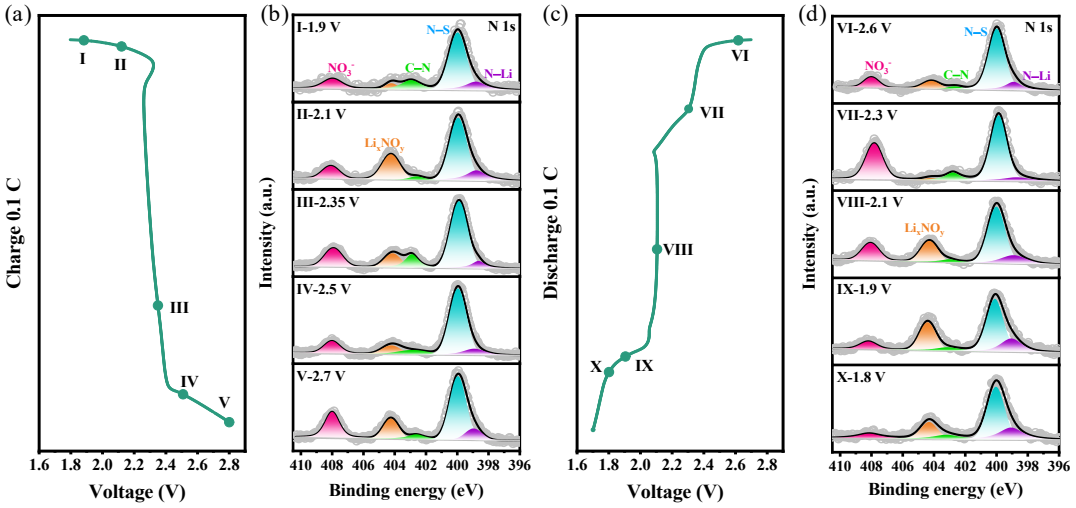

Fig. S48. (a) Galvanostatic charge profiles and (b) corresponding ex-situ N 1s XPS spectra analysis of V_{34}-DODA. (c) Galvanostatic discharge profiles and (d) corresponding ex-situ N 1s XPS spectra analysis of V_{34}-DODA.

Table S1. Element contents determined by EA and ICP.

Element	V	C	N	H
Content proportion (%)	19.96	50.17	1.56	7.83

Table S2. Performance comparison of Li-S batteries with V_{34}-DODA modified separator and other reported separator modification materials.

Sample	S Loading (mg cm^{-2})	Current density (C)	Cycles	Specific capacity (mAh g^{-1})	References
CoNi@ZnV_2O_4/ZnO-N,C-modified separator	1.1	1	900	533	[3]
		3	1000	467.9	
	4.2	0.1	30	897.1	
WP@NPC@PP	1.0	1	500	617	[4]
		3	1000	308	
	4.9	0.25	120	725	
FeS_2@TiO_2/PP	0.8-1.2	1	500	635	[5]
	3.9	0.1	50	890	
TiO-NFSs@PP	1.2	1	1000	516	[6]
	3.82	0.1	60	452.8	
	4.97	0.1	60	680	
CeO_2/Bi_2S_3-PP	0.9	0.5	100	853	[7]
		5	800	523	
MS-L separator	1-1.5	1	100	704.2	[8]
		2	500	548.9	
	4.6	0.5	50	574.4	
Mnx@NAC/PP	1-2	1	300	675	[9]
		4	300	483	
	4.6	0.5	100	650	
ZnV_2O_4-Li-MMT/PP	1.0-1.5	2	1000	432.2	[10]
		5	1000	361.1	
Ta_2O_5@rGO-PP	1.3	0.2	100	855	[11]
		1	700	485	
	4.5	0.1	100	736	
V_{34}-DODA modified separator	1.0	3	2000	480.8	**This work**
		5	2000	351.3	
	4.0	1	100	726.5	
	6.6	0.1	100	798.2	

References

[1] C. Zhang, M. Wang, C. Zhao, J. Wang, Y. Cao, L. Fan, H. Liu, G.-G. Gao, Enhanced selective oxidation of 5-hydroxymethylfurfural with a recyclable V_{34}@Fe_3O_4/C catalyst enriched with mixed-valence polyoxovanadate active centers, Fuel, 2025, 397, 135439.

[2] A. Müller, R. Rohlfing, J. Döring, M. Penk, Formation of a Cluster Sheath around a Central Cluster by a "Self-Organization Process": the Mixed Valence Polyoxovanadate $[V_{34}O_{82}]10^-$, Angew. Chem. Int. Ed., 1991, 30, 588-590.

[3] Z. Ouyang, B. Zheng, C. Shi, J. Li, W. Chen, J. Zhao, Y. Xiao, S. Lei, Baochang chengoxygen-defect-rich ZnV_2O_4/ZnO heterojunction as multifunctional separator to boost lithium polysulfide adsorption and conversion for superior lithium-sulfur batteries, J. Energy Storage, 2024, 94, 112405.

[4] C. Li, J. Yu, C. Zhang, D. Yang, J. Wang, H. Li, C. Huang, K. Xiao, Y. Cheng, Y. Ren, X. Qi, T. Yang, J. Li, J. Wang, G. Henkelman, J. Arbiol, J. Nan, A. Cabot, Tungsten phosphide on nitrogen and phosphorus-doped carbon as a functional membrane coating enabling robust lithium-sulfur batteries, J. Colloid Interface Sci., 2024, 670, 61-72.

[5] J. Song, L. Yue, Y. Dou, K. Yang, L. Zhang, L. Jiang, H. Liang, Y. Cao, T. Fan, X. Zhang, G. Qi, X. Sun, Z. Wang, Island-like FeS_2@TiO_2 heterojunction modified separator for enhanced polysulfide management in lithium-sulfur batteries, Chem. Eng. J., 2025, 511, 161934.

[6] W. Zhang, J. Xue, J. Zhang, Y. Ge, N. Zhu, Z. Lei, X. He, Q. Li, Z. Liu, J. Sun,

Synergistic cation-anion vacancies and topological morphology tuning on TiO nanoflower spheres for efficient polysulfide confinement and catalysis in lithium sulfur batteries, Small, 2026, 0, e14502.

[7] Q. Ren, Z. Wang, B. Jin, Dual-effect interface layer built by heterostructure suppresses polysulfide shuttling, Sustain. Mater. Technol., 2026, 48, e02057.

[8] F. Guo, Y. Jin, F. Cao, Y. Guo, W.-C. Li, Y. Song, D.-C. Guo, B. He, A.-H. Lu, Ultrathin MnO_2 nanosheets coated multifunctional separator for lithium-sulfur batteries showing high stability, ChemSusChem, 2026, 19, e70652.

[9] C.-A. Zhou, J. Zhou, S. Cai, X. Li, Y. Tang, Y. Yu, J. Xie, L. Song, C. Wang, K. Ma, H. Yue, Enhancing lithium-sulfur batteries performance with Mn atomic clusters modified separator via promoting polysulfide conversion, ACS Appl. Mater. Interfaces, 2026, 18, 23017-23027.

[10] X. Li, J. Zhu, R. Sheng, T. Xu, K. Chen, J. Ding, Y. Huang, Defect-mediated dual role interfaces enables the sulfur reduction reaction kinetics for highly stable lithium sulfur batteries, Chem. Eng. J., 2025, 525, 170497.

[11] A. E. Shrshr, B. Miao, M. M. Elsenety, M. S. Nadeem, M. Asad, I. A. Mir, L. Rasheed, A. Z. Alhakemy, M. Yasir, J. Bai, J. Zhang, M. A. Al-Tahan, Synthesis of Ta_2O_5@rGO nanohybrid via a unique one-step hydrothermal approach as an efficient separator modifier for lithium-sulfur batteries, J. Power Sources, 2026, 665, 239043.